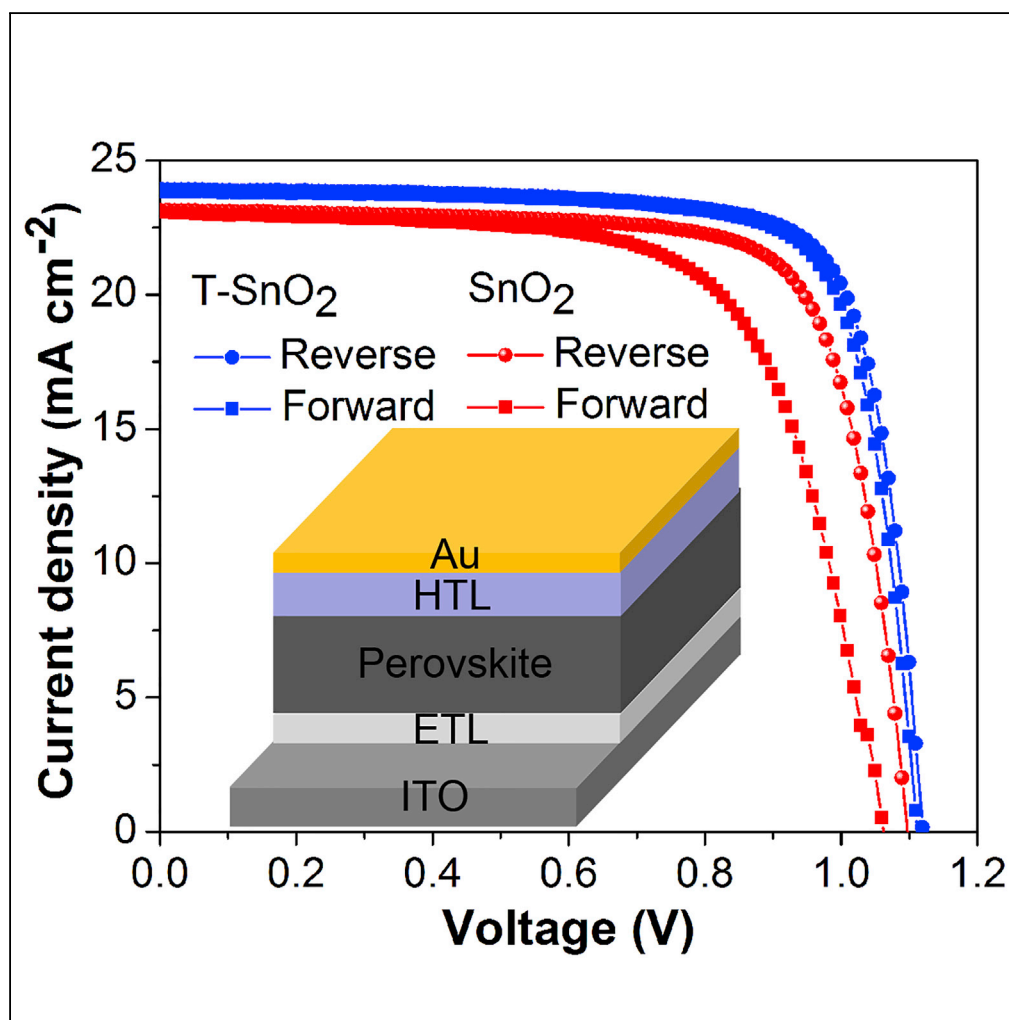## Article

High-Performance Planar Perovskite Solar Cells with Negligible Hysteresis Using 2,2,2-Trifluoroethanol-Incorporated SnO$_2$

Yigang Luan, Xiaohui Yi, Peng Mao, ..., Tao Lin, Cheng Li, Jizheng Wang

jizheng@iccas.ac.cn

HIGHLIGHTS

An effective trifluoroethanol-incorporated SnO$_2$ (T-SnO$_2$) ETL is applied to PSCs

The T-SnO$_2$ ETL exhibits improved electron mobility and optimized work function

The PSC displays PCE of 20.92% and negligible hysteresis

PCE is improved to 21.68% by O$_2$ plasma treating the T-SnO$_2$ ETL

iScience

Article

High-Performance Planar Perovskite Solar Cells with Negligible Hysteresis Using 2,2,2-Trifluoroethanol-Incorporated SnO$_2$

Yigang Luan,[1,2] Xiaohui Yi,[3] Peng Mao,[1,2] Yuanzhi Wei,[1,2] Jing Zhuang,[1,2] Ningli Chen,[1,2] Tao Lin,[1] Cheng Li,[3] and Jizheng Wang[1,2,4,*]

SUMMARY

An efficient electron transport layer (ETL) between the perovskite absorber and the cathode plays a crucial role in obtaining high-performance planar perovskite solar cells (PSCs). Here, we incorporate 2,2,2-trifluoroethanol (TFE) in the commonly used tin oxide (SnO$_2$) ETL, and it successfully improves the power conversation efficiency (PCE) and suppresses the hysteresis of the PSCs: the PCE is increased from 19.17% to 20.92%, and the hysteresis is largely reduced to be almost negligible. The origin of the enhancement is due to the improved electron mobility and optimized work function of the ETL, together with the reduced traps in the perovskite film. In addition, O$_2$ plasma is employed to treat the surface of the TFE-incorporated SnO$_2$ film, and the PCE is further increased to 21.68%. The concept here of incorporating organic small molecules in the ETL provides a strategy for enhancing the performance of the planar PSCs.

INTRODUCTION

Lead halide perovskite solar cells (PSCs) have attracted great attention for their high efficiency, high defect tolerance, and low cost (Wang et al., 2017a; Liu et al., 2015; Stranks et al., 2013; Chen et al., 2017a; Bush et al., 2016; Ono et al., 2017). Recently, the reported efficiency has exceeded 23% by optimizing the interface, perovskite thin film, and perovskite absorber materials (Jiang et al., 2019; Yang et al., 2018a; Jeon et al., 2015). Among the PSCs, planar ones are drawing more and more interest owing to their relatively simpler fabrication (in comparison with the mesoporous PSCs) (Jiang et al., 2019; Yang et al., 2018b).

In a typical planar PSC, the perovskite absorber is usually placed between the hole transport layer (HTL) and the electron transport layer (ETL). Generally, the commonly used HTLs are 2,2′,7,7′-tetrakis-(N,N-di-4-methoxyphenylamine)-9,9′-spirobifluorene (Spiro-OMeTAD) and poly [bis (4-phenyl) (2,4,6-trimethylphenyl) amine] (PTAA), which have been proved to be efficient HTLs with high hole mobility and remarkable electron-blocking property (Heo et al., 2015). For ETLs, TiO$_2$ is a typically used one, especially for high efficiency n-i-p type PSCs (Zhou et al., 2014; Jeon et al., 2018; Peng et al., 2017; Tan et al., 2017). However, the strong catalytic effect of TiO$_2$ can damage the stability of the PSCs under light illumination (Shin et al., 2017; Luo et al., 2018). Thereby researchers are seeking for other n-type metal oxides for better choice. SnO$_2$ can be processed into both compact and mesoporous films (Dong et al., 2015), and the films have high transparency in the visible region and good energy level alignment with the perovskite. Nowadays SnO$_2$ ETLs are widely used in PSCs to achieve high power conversation efficiencies (PCEs) (Ke et al., 2015; Wang et al., 2016; Chen et al., 2017b; Jiang et al., 2016).

However, many reports have shown that the PSCs based on the pure SnO$_2$ ETL still have serious hysteresis and unsatisfactory performance (Dong et al., 2017; Zhu et al., 2016; Bu et al., 2018; Wei et al., 2018). These problems are attributed to low electron mobility of the SnO$_2$ ETL and high trap-state density in the perovskite device (Bai et al., 2017; Schulz et al., 2019; Xiong et al., 2018; Wang et al., 2018a; Xie et al., 2017). Thereby researchers are finding efficient ways of modifying the pure SnO$_2$ layer to solve the problems. For examples, Ke et al. put a very thin PCBM layer on the SnO$_2$ layer to promote electron transport and suppress interface carrier recombination (Ke et al., 2016), Yang et al. made EDTA-complexed SnO$_2$ ETL to improve the electron mobility (Yang et al., 2018b), and several other groups used self-assembled monolayers (SAMs) to passivate the interfacial trap sites (Yang et al., 2017; Zuo et al., 2017). These methods all lead to enhanced performances.

[1]Beijing National Laboratory for Molecular Sciences, CAS Key Laboratory of Organic Solids, Institute of Chemistry, Chinese Academy of Sciences, Beijing 100190, P. R. China

[2]University of Chinese Academy of Sciences, Beijing 100049, P. R. China

[3]Semiconductor Photonics Research Center, OSED, Department of Physics, Jiujiang Research Institute, Xiamen University, Xiamen, Fujian 361005, P. R. China

[4]Lead Contact

*Correspondence: jizheng@iccas.ac.cn

https://doi.org/10.1016/j.isci.2019.06.004

Here, we made 2,2,2-trifluoroethanol (TFE)-incorporated SnO_2 (T-SnO_2) ETL by incorporating TFE (Meng et al., 2018), a water-soluble organic small molecule with strong electron-withdrawing group (trifluoromethyl) into the SnO_2 colloidal water solution. Consequently, the electron mobility in the SnO_2 ETL is largely improved and trap states in the perovskite absorber is greatly reduced. As a result, the hysteresis is obviously eliminated and a high PCE of 20.92% is achieved. Furthermore, we employed O_2 plasma to treat the surface of the T-SnO_2 film, and a superior PCE of 21.68% is obtained.

RESULTS AND DISCUSSION

Characterization of T-SnO_2

The transmission electron microscopy images of the SnO_2 and T-SnO_2 nanoparticles are shown in Figure S1. For the pristine SnO_2 particles, large-size clusters (50–70 nm) can be clearly seen; this is due to the aggregation of the SnO_2 nanoparticles when they were in solution. For the T-SnO_2 particles, the size is about 3–5 nm. The much smaller size is attributed to the strong electron-withdrawing property of the trifluoromethyl group in TFE, which greatly restricts the aggregation of the SnO_2 nanoparticles in solution. X-ray photoelectron spectroscopy (XPS) was used to elucidate the state of the F and Sn in the SnO_2 and T-SnO_2 films coated on indium tin oxide (ITO) substrates. In Figure 1A, it is found that F 1s peak of the T-SnO_2 film locates at ~684.1 eV, which is consistent with the value in the literature (Wang et al., 2017b; Kim et al., 2018). In contrast, there is no associated peak for the SnO_2 film. In Figure 1B, it is found that the Sn 3d peaks of the T-SnO_2 film shift to lower binding energy by about 0.36 eV in contrast to that of the SnO_2 film. Fourier transform infrared (FTIR) spectrum demonstrates that the T-SnO_2 nanoparticles contain the characterization peaks of both TFE and SnO_2 (Figure S2). All the aforementioned tests strongly indicate that the TFE is effectively incorporated in the SnO_2 film.
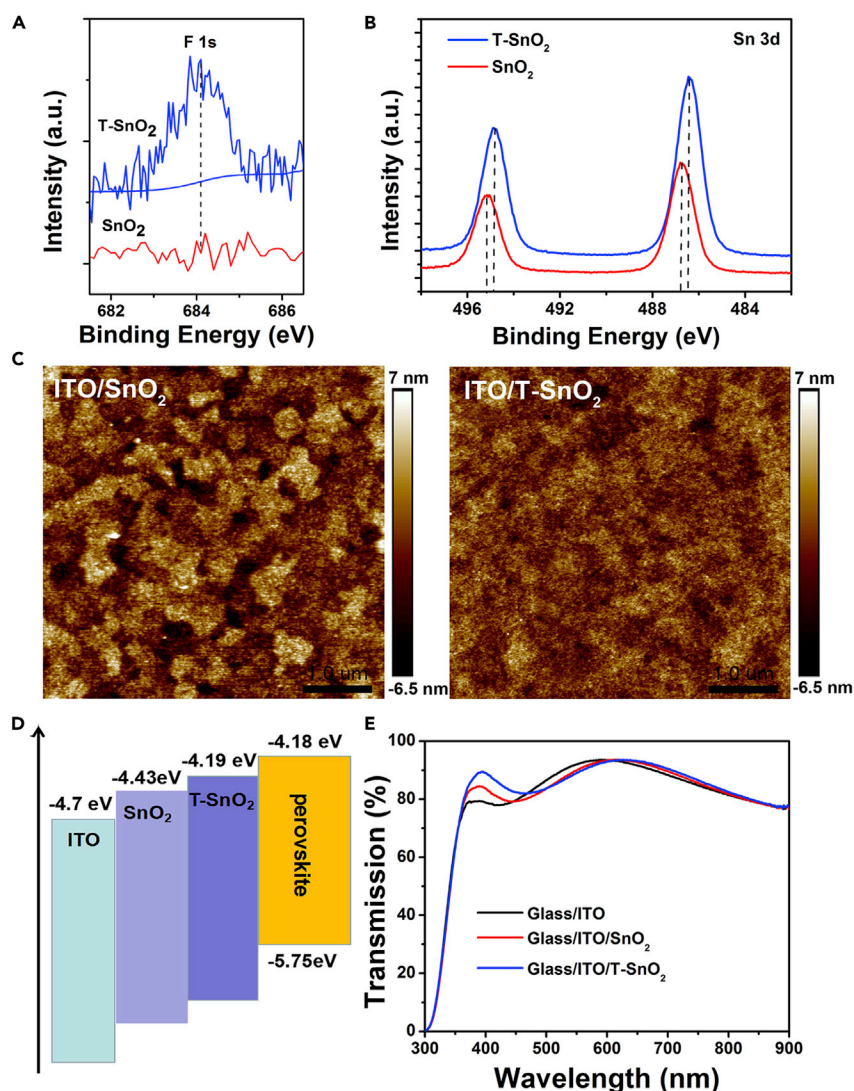
Atomic force microscopy (AFM) was performed to compare the roughness of the T-SnO_2 and SnO_2 films. As shown in Figure 1C, the roughness of the T-SnO_2 film (root mean square [RMS]: 1.70 nm) is less than that of the SnO_2 film (RMS: 2.17 nm). The smoother surface is beneficial for later perovskite film growth and a better contact with the T-SnO_2 ETL. In addition, UV photoelectron spectroscopy (UPS) measurement was carried out to estimate the work function (WF) of the SnO_2 and T-SnO_2 films (Figure S3). Figure 1D shows the energy levels of the perovskite film and the two ETLs. It is seen that the WF of the T-SnO_2 film is closer to the conduction band of the perovskite film (Figure S4) in comparison with that of the SnO_2 film, which is beneficial for increasing V_{oc} (Wang et al., 2018b; Yang et al., 2016; Yu et al., 2018).

Figure 1E compares the optical transmission spectra of the SnO_2 and T-SnO_2 films. It is seen that all the samples display good transparency in the visible region. In addition, the T-SnO_2 film exhibits a higher electron mobility (6.17×10^{-3} cm^2 V^{-1} s^{-1}) than that of the SnO_2 film (2.10×10^{-3} cm^2 V^{-1} s^{-1}), as measured by the space charge limited current (SCLC) method (Figure S5) (Jiang et al., 2016; Yu et al., 2018).

Structure and Performance of PSCs

We then fabricated planar PSCs with the T-SnO_2 and the SnO_2 ETLs in an architecture of glass/ITO/ETL/perovskite/Spiro-OMeTAD/Au. The cross-sectional scanning electron microscopy (SEM) of the T-SnO_2 device is shown in Figure 2A, in which each layer is clearly seen. The ~680-nm-thick perovskite layer is coated on the ETL substrates using the widely adopted two-step method (more details are shown in Transparent Methods) (Jiang et al., 2016; Wang et al., 2018b). SEM top view of the perovskite films grown on the two ETLs are provided in Figure S6; it is seen that both films are pinhole-free and uniform and contain similar crystal grains. The grain sizes are ~750 nm. X-ray diffraction (XRD) measurements (Figure S7) also give very similar results for the two perovskite films (Wang et al., 2018b; Jiang et al., 2017; Chen et al., 2014; Kim et al., 2016). These studies confirm that TFE has a negligible effect on the perovskite crystallization.

The device performance is optimized by varying the TFE volume and the annealing temperature for the ETL. The PCE reaches a maximum when the TFE volume increases to 350 μL (Figure S8 and Table S1). The optimal annealing temperature is 130°C for the T-SnO_2 film (Figure S9). Figure 2B indicates the J-V curves of the best SnO_2 and T-SnO_2 devices, and the device parameters are shown in Table 1. The SnO_2 device displays quite obvious hysteresis: under reverse scan direction, it has a PCE of 19.17% (V_{oc}: 1.10 V, J_{sc}: 23.12 mA cm^{-2}, and FF: 0.755); under forward scan direction, it has a PCE of 16.47% (V_{oc}: 1.06 V, J_{sc}: 23.03 mA cm^{-2} and FF: 0.674). In contrast, the T-SnO_2 device presents negligible hysteresis: under reverse scan, it has a PCE of 20.92% (V_{oc}: 1.12 V, J_{sc}: 23.91 mA cm^{-2} and FF: 0.780); under forward scan, it has a PCE of 20.62% (V_{oc}: 1.11 V, J_{sc}: 23.87 mA cm^{-2} and FF: 0.777). We conducted statistical studies for the SnO_2 and T-SnO_2 devices. Fifty PSCs were made for each, and the results are given in Figure S10.

Figure 1. The Characterizations of the ITO/SnO$_2$ and ITO/T-SnO$_2$ Films

(A and B) XPS spectra of F 1s peak (A) and Sn 3d peaks (B).

(C) AFM images of the SnO$_2$ (*left*) and T-SnO$_2$ (*right*) films.

(D) Schematic diagram of work functions of the ITO/SnO$_2$ and ITO/T-SnO$_2$ relative to the conduction band of the perovskite film.
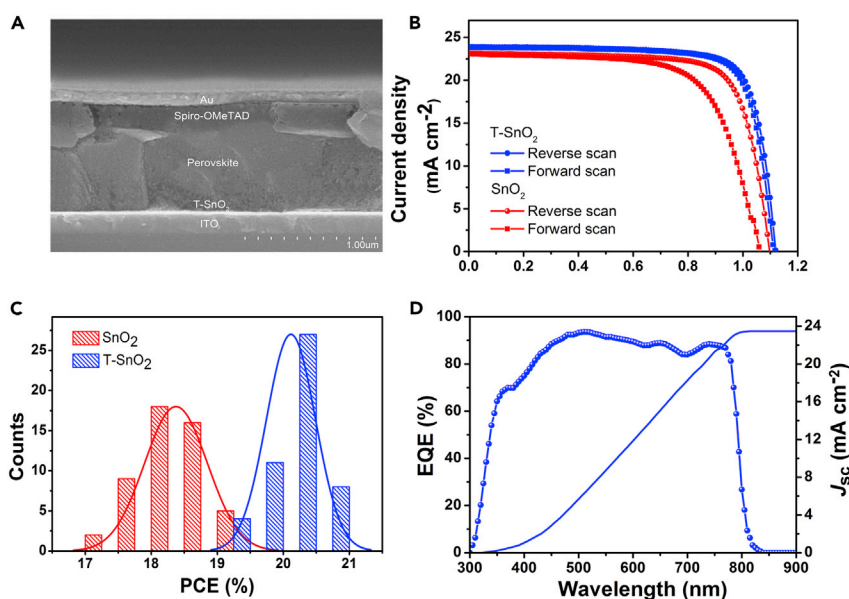
(E) Optical transmission of the ITO, ITO/SnO$_2$, and ITO/T-SnO$_2$ on the glass substrates.

For the 50 SnO$_2$ devices, the average PCE, V_{oc}, J_{sc}, and *FF* are 18.38%, 1.09 V, 22.91 mA cm^{-2}, and 0.734, respectively, whereas for the 50 T-SnO$_2$ devices, the corresponding values are 20.12%, 1.11 V, 23.66 mA cm^{-2}, and 0.764. The larger V_{oc} can be attributed to the better-aligned energy levels of the T-SnO$_2$ and perovskite layers. The higher *FF* and J_{sc} are likely due to the improved electron mobility. In addition, the T-SnO$_2$ devices exhibit a narrower distribution of PCE (19%–21% versus 17%–20%), indicating their excellent reproducibility (Figure 2C). All the above-mentioned statistical results confirm the advantage of the T-SnO$_2$ ETL. The external quantum efficiency (EQE) spectra of the T-SnO$_2$ device is exhibited in Figure 2D, and the integrated J_{sc} for the T-SnO$_2$ device is 23.48 mA cm^{-2}, which is consistent with the J_{sc} of 23.91 mA cm^{-2} obtained from the *J-V* result (within 2% deviation).

Charge Transport Studies

To study the trap density, the SCLC model was adopted with the electron-only devices (ITO/ETL/perovskite/PCBM/Ag) (Chen et al., 2017b). Figure 3A shows the dark *I-V* curves of the two devices. Generally,

Figure 2. Structure and Performance of the PSCs

(A) Cross-sectional SEM of the T-SnO$_2$ device.

(B) *J-V* curves at both forward (*solid square*) and reverse (*solid circle*) scans of the best SnO$_2$ and T-SnO$_2$ devices.

(C) PCE performance distribution of 50 SnO$_2$ or 50 T-SnO$_2$ devices.

(D) EQE spectrum of the T-SnO$_2$ device.

at low bias voltage, the *I-V* curve shows linear ohmic-type response. With the increase of the bias voltage, the current starts to increase nonlinearly, indicating the trap filling process is triggered. The kink point between the linear region and the nonlinear region is defined as trap-filled limit voltage (V_{TFL}), and the trap density (N_t) can be calculated using the following Equation 1:
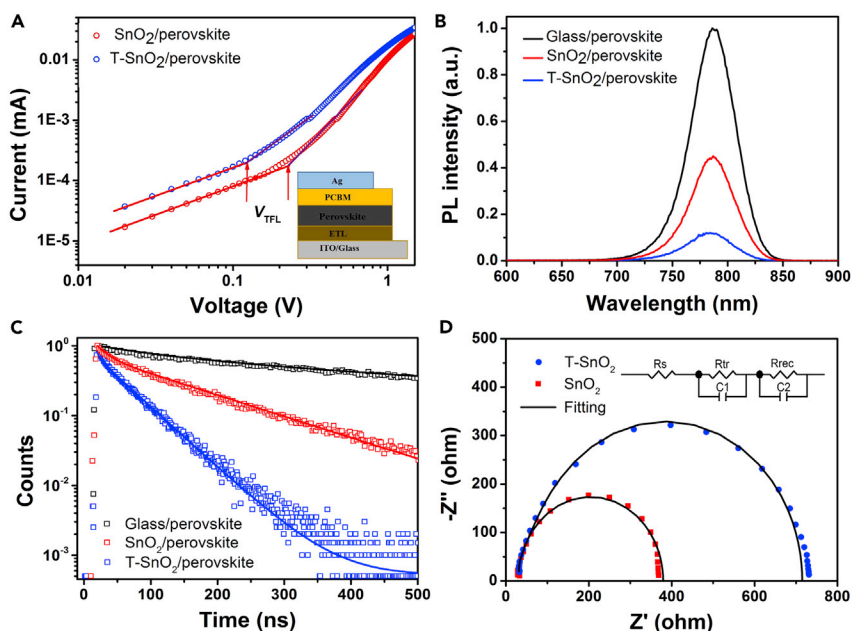
$$N_t = \frac{2\varepsilon_0\varepsilon V_{TFL}}{eL^2}$$

(Equation 1)

where ε_0, ε, e, and L are permittivity of vacuum, relative dielectric constant, elementary charge, and perovskite film thickness, respectively. The calculated trap density of the perovskite film on the T-SnO$_2$ ETL is about 8.94×10^{15} cm^{-3}, much lower than that of the perovskite film deposited on the SnO$_2$ ETL (1.95×10^{16} cm^{-3}).

Figure 3B shows the steady-state photoluminescence (PL) spectra of the perovskite films coated on bare glass and the SnO$_2$ and T-SnO$_2$ ETLs. It is seen that the perovskite film on the T-SnO$_2$ ETL gives most significant PL quenching, indicating very efficient electron transfer from the perovskite film to the T-SnO$_2$ ETL. This is due to the reduced trap density in the perovskite film and enhanced electron mobility in the T-SnO$_2$ ETL. Time-resolved photoluminescence (TRPL) of the three samples are given in Figure 3C, from which carrier lifetime can be calculated. The carrier lifetime of the Glass/perovskite, SnO$_2$/perovskite, and T-SnO$_2$/perovskite samples are ~763, 147, and 52 ns, respectively (Table S2). The significantly reduced carrier lifetime of the perovskite/T-SnO$_2$ sample strongly indicates a fast electron transfer from the perovskite film into the T-SnO$_2$ film, hence carrier recombination can be greatly suppressed (Zhu et al., 2014; Liang et al., 2014).

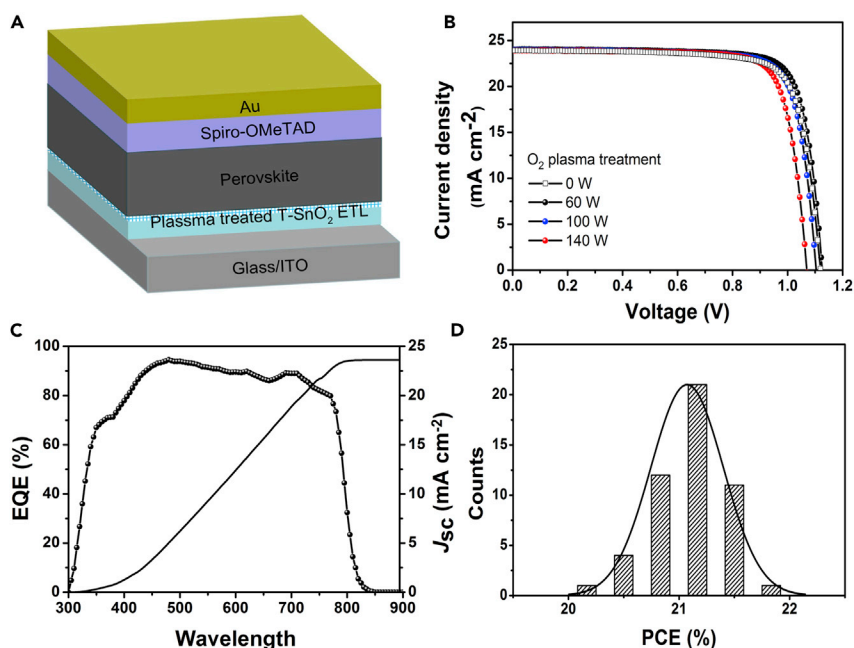| ETL	Scan Direction	V_{oc} (V)	J_{sc} (mA cm^{-2})	FF (−)	PCE (%)
SnO$_2$	Reverse	1.10	23.12	0.755	19.17
	Forward	1.06	23.03	0.674	16.47
T-SnO$_2$	Reverse	1.12	23.91	0.780	20.92
	Forward	1.11	23.87	0.777	20.62

Table 1. Performances of the SnO$_2$ and T-SnO$_2$ Devices

Figure 3. Charge Transport Properties Studies

(A) Dark *I-V* measurement of the electron-only devices based on SnO_2 and $T-SnO_2$ ETLs (inserted picture).

(B and C) PL (B) and TRPL (C) spectra of the perovskite films coated on Glass, SnO_2, and $T-SnO_2$, respectively.

(D) EIS spectra of the SnO_2 and $T-SnO_2$ devices in dark with a bias of −1 V.

Figure 3D shows the Nyquist plots of the impedance spectroscopy (EIS) for the SnO_2 and $T-SnO_2$ devices; the equivalent circuit is also shown. R_{tr} is charge transfer resistance; R_{rec} is recombination resistance (Yang et al., 2015; Li et al., 2015; Jin et al., 2016). The extracted R_{tr} and R_{rec} are listed in Table S3. It is seen that the $T-SnO_2$ device has larger R_{rec} (650.5 vs 294.2), meaning a weaker carrier recombination in the perovskite film. The $T-SnO_2$ device has a smaller R_{tr} (36.8 vs 56.4), meaning a more efficient electron transfer process from the perovskite film to the ETL. The EIS results are consistent with the above-mentioned trap density, PL, and TRPL analysis. All the results presented in Figure 3 are in good agreement with the enhanced PCE and the remarkable negligible hysteresis of the $T-SnO_2$ device.

Oxygen Plasma Treatment

Oxygen plasma is usually used to treat the ITO or (FTO) surface in fabrication of planar PSCs (Minarik and Vana, 2015; Dao et al., 2015; Tang et al., 2018; Huang et al., 2017). Here, we use O_2 plasma to treat the surface of the $T-SnO_2$ ETL. The O_2 gas flow rate is fixed at 0.05 L h^{-1}, and the power varies. The treated ETL is named $p-T-SnO_2$ ETL. Figure 4A shows the structure of the $p-T-SnO_2$ device (ITO/$p-T-SnO_2$/Perovskite/ Spiro-OMeTAD/Au), and a cross-section SEM is exhibited in Figure S11. The FTIR and XPS results show that the F mainly exists in TFE state in the $p-T-SnO_2$ ETL (Figure S12). Figure 4B shows the *J-V* curves of the $p-T-SnO_2$ devices (with different plasma powers); the device parameters are shown in Table S4. The champion device exhibits a PCE of 21.68% (V_{oc}: 1.12 V, J_{sc}: 24.06 mA cm^{-2}, and *FF*: 0.802), which is higher than the best $T-SnO_2$ device. The improvement can be attributed to the smoother surface of the $p-T-SnO_2$ film, which is indicated by AFM measurements (Figure S13 and Table S5): the roughness of the $p-T-SnO_2$ ETL is 1.13 nm and that of the $T-SnO_2$ ETL is 1.67 nm. The very high *FF* of larger than 0.80 should have resulted from the improved interface between the $p-T-SnO_2$ ETL and the perovskite film. As depicted in Figure 4B, V_{oc} decreases from 1.12 to 1.07 V as the power increases from 60 to 140 W; this can be explained by the plasma-caused WF change of the $T-SnO_2$ ETL (Figure S14 and Table S6): the WF is going down (from 4.21 to 4.40 eV) away from the conduction band of the perovskite film (4.18 eV). Figure 4C shows the EQE and integrated J_{sc} (23.61 mA cm^{-2}) of the $p-T-SnO_2$ device, which is consistent with the J_{sc} of 24.06 mA cm^{-2} obtained from *J-V* measurement (with 2% deviation). Statistical study was conducted for 50 $p-T-SnO_2$ devices, and the PCE distribution is shown in Figure 4D. The PCE ranges from 20% to 22%, and most of the devices are among the >21% range, indicating very good reproducibility of the $p-T$-SnO_2 devices.

Figure 4. Oxygen Plasma Treatment

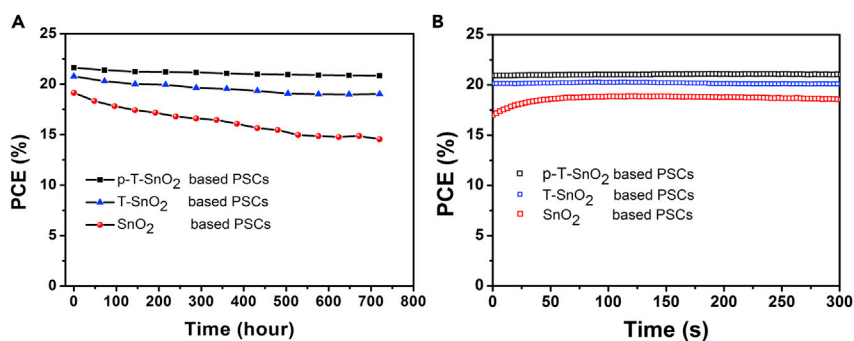(A) Schematic illustrations of the architecture of the p-T-SnO$_2$ device.

(B) J-V curves of the p-T-SnO$_2$ devices with different plasma power.

(C) EQE spectrum of the 60-W plasma-treated devices.

(D) PCE distribution for the 60-W plasma-treated devices.

Stability Tests

The long-term stabilities of the SnO$_2$, T-SnO$_2$, and p-T-SnO$_2$ devices were measured without any encapsulation. Figure 5A shows PCE vs time in 720-h dark condition storage (RH 30%–40%); it is seen that the SnO$_2$ device maintains only 76% of its initial PCE, whereas the T-SnO$_2$ and p-T-SnO$_2$ devices retain over 90% of their initial PCEs. The enhanced stability is due to improved interface binding strength induced by the TFE modification and plasma treatment (Tress et al., 2016; Tan et al., 2017). Figure 5B shows the steady-state efficiency of the devices under MPP (maximum power point) conditions. It is seen that the SnO$_2$ device takes about 50 s to reach the maximum photocurrent, likely owing to a trap-filling process or ion migration (Wei et al., 2018; deQuilettes et al., 2016). Its PCE then stabilizes at about 18.6%, whereas the PCEs of the T-SnO$_2$ and p-T-SnO$_2$ devices immediately stabilize at about 20.1% and 21.0%, respectively. The stability test clearly indicates the advantage of the T-SnO$_2$ and p-T-SnO$_2$ ETLs.

Figure 5. Stability Tests for the SnO$_2$, T-SnO$_2$, p-T-SnO$_2$ Devices without any Encapsulation

(A) Air stability (30%–40% RH).

(B) Maximum power point tracking.

Conclusion

In conclusion, we present a simple, low-cost method by introducing TFE in the SnO_2 colloidal solution and achieved an effective ETL. The T-SnO_2 ETL exhibits improved electron mobility, suitable energy levels that aligned well with that of the perovskite film. The ETL also shows a very smooth surface, which allows high-quality perovskite film growth and ensures a good ETL/perovskite interface. As a result, the trap density at the interface and inside the perovskite absorber is greatly reduced, leading to largely suppressed carrier recombination. As a result, the device displays an improved PCE of 20.92% with negligible hysteresis. In addition, the surface of T-SnO_2 film is further optimized by O_2 plasma treatment, and a higher PCE of 21.68% is obtained, together with a very high *FF* of larger than 0.80. Moreover, the devices with T-SnO_2 ETLs exhibit excellent stability. The simple and economical method provides an insightful strategy for preparing efficient ETLs for future PSCs.

Limitations of the Study

In this study, we found that the fluorine was incorporated into the perovskite crystal at T-SnO_2/perovskite interface (Figure S15), which might contribute to the defects passivation. However, we do not have convincing evidence for this. More studies are needed to reveal the role of fluorine at the ETL/perovskite interface.

METHODS

All methods can be found in the accompanying Transparent Methods supplemental file.

SUPPLEMENTAL INFORMATION

Supplemental Information can be found online at https://doi.org/10.1016/j.isci.2019.06.004.

AUTHOR CONTRIBUTIONS

Y.L., P.M., Y.W., J.Z., T.L., and J.W. conceived the idea. Y.L., X.Y., and J.W. designed the experiments. Y.L. fabricated the devices and carried out the majority of measurements. J.Z. conducted the SEM and PL experiments. Y.W. conducted the AFM experiments. N.C. conducted the EIS experiments. X.Y., C.L., P.M., and T.L. assisted in data analysis. Y.L. and J.W. wrote the manuscript and interpreted the data.

DECLARATION OF INTERESTS

The authors declare no competing interests.

REFERENCES

Bai, Y., Meng, X., and Yang, S. (2017). Interface engineering for highly efficient and stable planar p-i-n perovskite solar cells. Adv. Energy Mater. *8*, 1701883.

Bu, T., Li, J., Zheng, F., Chen, W., Wen, X., Ku, Z., Peng, Y., Zhong, J., Cheng, Y.-B., and Huang, F. (2018). Universal passivation strategy to slot-die printed SnO_2 for hysteresis-free efficient flexible perovskite solar module. Nat. Commun. *9*, 4609.

Bush, K.A., Bailie, C.D., Chen, Y., Bowring, A.R., Wang, W., Ma, W., Leijtens, T., Moghadam, F., and McGehee, M.D. (2016). Thermal and environmental stability of semi-transparent perovskite solar cells

for tandems enabled by a solution-processed nanoparticle buffer layer and sputtered ito electrode. Adv. Mater. *28*, 3937–3943.

Chen, Q., Zhou, H., Song, T.-B., Luo, S., Hong, Z., Duan, H.-S., Dou, L., Liu, Y., and Yang, Y. (2014). Controllable self-induced passivation of hybrid lead iodide perovskites toward high performance solar cells. Nano Lett. *14*, 4158–4163.

Chen, H., Ye, F., Tang, W., He, J., Yin, M., Wang, Y., Xie, F., Bi, E., Yang, X., Grätzel, M., et al. (2017a). A solvent- and vacuum-free route to large-area perovskite films for efficient solar modules. Nature *550*, 92–95.

Chen, H., Liu, D., Wang, Y., Wang, C., Zhang, T., Zhang, P., Sarvari, H., Chen, Z., and Li, S. (2017b). Enhanced performance of planar perovskite solar cells using low-temperature solution-processed Al-doped SnO_2 as electron transport layers. Nanoscale Res. Lett. *12*, 6.

Dao, V.-D., Larina, L.L., and Choi, H.-S. (2015). Minimizing energy losses in perovskite solar cells using plasma-treated transparent conducting layers. Thin Solid Films *593*, 10–16.

deQuilettes, D.W., Zhang, W., Burlakov, V.M., Graham, D.J., Leijtens, T., Osherov, A., Bulović, V., Snaith, H.J., Ginger, D.S., and Stranks, S.D. (2016). Photo-induced halide redistribution in

organic-inorganic perovskite films. Nat. Commun. 7, 11683.

Dong, Q., Shi, Y., Wang, K., Li, Y., Wang, S., Zhang, H., Xing, Y., Du, Y., Bai, X., and Ma, T. (2015). Insight into perovskite solar cells based on SnO$_2$ compact electron-selective layer. J. Phys. Chem. C 119, 10212–10217.

Dong, Q., Shi, Y., Zhang, C., Wu, Y., and Wang, L. (2017). Energetically favored formation of SnO$_2$ nanocrystals as electron transfer layer in perovskite solar cells with high efficiency exceeding 19%. Nano Energy 40, 336–344.

Heo, J.H., Han, H.J., Kim, D., Ahn, T.K., and Im, S.H. (2015). Hysteresis-less inverted CH$_3$NH$_3$PbI$_3$ planar perovskite hybrid solar cells with 18.1% power conversion efficiency. Energy Environ. Sci. 8, 1602–1608.

Huang, F., Wei, Y., Gu, L., Guo, Q., Xu, H., Luo, D., Jin, S., Yang, X., Huang, Y., and Wu, J. (2017). Interface engineering of electron transport layer-free planar perovskite solar cells with efficiency exceeding 15 %. Energy Technol. 5, 1844–1851.

Jeon, N.J., Noh, J.H., Yang, W.S., Kim, Y.C., Ryu, S., Seo, J., and Seok, S.I. (2015). Compositional engineering of perovskite materials for high-performance solar cells. Nature 517, 476–480.

Jeon, N.J., Na, H., Jung, E.H., Yang, T.-Y., Lee, Y.G., Kim, G., Shin, H.-W., Seok, S.I., Lee, J., and Seo, J. (2018). A fluorene-terminated hole-transporting material for highly efficient and stable perovskite solar cells. Nat. Energy 3, 682–689.

Jiang, Q., Zhang, L., Wang, H., Yang, X., Meng, J., Liu, H., Yin, Z., Wu, J., Zhang, X., and You, J. (2016). Enhanced electron extraction using SnO$_2$ for high-efficiency planar-structure HC(NH$_2$)$_2$PbI$_3$-based perovskite solar cells. Nat. Energy 2, 16177.

Jiang, Q., Chu, Z., Wang, P., Yang, X., Liu, H., Wang, Y., Yin, Z., Wu, J., Zhang, X., and You, J. (2017). Planar-structure perovskite solar cells with efficiency beyond 21%. Adv. Mater. 29, 1703852.

Jiang, Q., Zhao, Y., Zhang, X., Yang, X., Chen, Y., Chu, Z., Ye, Q., Li, X., Yin, Z., and You, J. (2019). Surface passivation of perovskite film for efficient solar cells. Nat. Photon. https://doi.org/10.1038/s41566-019-0398-2.

Jin, Z., Wang, A., Zhou, Q., Wang, Y., and Wang, J. (2016). Detecting trap states in planar pbs colloidal quantum dot solar cells. Sci. Rep. 6, 37106.

Ke, W.J., Fang, G.J., Liu, Q., Xiong, L.B., Qin, P.L., Tao, H., Wang, J., Lei, H.W., Li, B.R., Wan, J.W., et al. (2015). Low-temperature solution-processed tin oxide as an alternative electron transporting layer for efficient perovskite solar cells. J. Am. Chem. Soc. 137, 6730–6733.

Ke, W., Zhao, D., Xiao, C., Wang, C., Cimaroli, A.J., Grice, C.R., Yang, M., Li, Z., Jiang, C.-S., Al-Jassim, M., et al. (2016). Cooperative tin oxide fullerene electron selective layers for high-performance planar perovskite solar cells. J. Mater. Chem. A 4, 14276–14283.

Kim, Y.C., Jeon, N.J., Noh, J.H., Yang, W.S., Seo, J., Yun, J.S., Ho-Baillie, A., Huang, S., Green, M.A., Seidel, J., et al. (2016). Beneficial effects of

PbI$_2$ incorporated in organo-lead halide perovskite solar cells. Adv. Energy Mater. 6, 1502104.

Kim, J.-H., Yonezawa, S., and Okada, T. (2018). Effects of surface fluorination on the dispersion stability and the electrical conductivity of SnO$_2$ particles using fluorine gas. Chem. Lett. 47, 393–395.

Li, H., Cao, J., Zhou, Q., Ding, L., and Wang, J. (2015). High-performance inverted PThTPTI: PC$_{71}$BM solar cells. Nano Energy 15, 125–134.

Liang, P.-W., Liao, C.-Y., Chueh, C.-C., Zuo, F., Williams, S.T., Xin, X.-K., Lin, J., and Jen, A.K.-Y. (2014). Additive enhanced crystallization of solution-processed perovskite for highly efficient planar-heterojunction solar cells. Adv. Mater. 26, 3748–3754.

Liu, Y., Yang, Z., Cui, D., Ren, X., Sun, J., Liu, X., Zhang, J., Wei, Q., Fan, H., Yu, F., et al. (2015). Two-inch-sized perovskite CH3NH3PbX3 (X = Cl, Br, I) crystals: growth and characterization. Adv. Mater. 27, 5176–5183.

Luo, J., Chen, J., Wu, B., Goh, T.W., Qiao, W., Ku, Z., Yang, H.B., Zhang, L., Sum, T.C., and Liu, B. (2018). Surface reutilization of anatase TiO$_2$ for efficient electron extraction and stable P$_{max}$ output of perovskite solar cells. Chem 4, 911–923.

Meng, X., Ho, C.H.Y., Xiao, S., Bai, Y., Zhang, T., Hu, C., Lin, H., Yang, Y., So, S.K., and Yang, S. (2018). Molecular design enabled reduction of interface trap density affords highly efficient and stable perovskite solar cells with over 83% fill factor. Nano Energy 52, 300–306.

Minarik, S., and Vana, D. (2015). Applicability of random sequential adsorption algorithm for simulation of surface plasma polishing kinetics. Appl. Surf. Sci. 355, 364–368.

Ono, L.K., Park, N.-G., Zhu, K., Huang, W., and Qi, Y. (2017). Perovskite solar cells-towards commercialization. ACS Energy Lett. 2, 1749–1751.

Peng, J., Duong, T., Zhou, X., Shen, H., Wu, Y., Mulmudi, H.K., Wan, Y., Zhong, D., Li, J., Tsuzuki, T., et al. (2017). Efficient Indium-doped TiO$_x$ electron transport layers for high-performance perovskite solar cells and perovskite-silicon tandems. Adv. Mater. 7, 1601768.

Schulz, P., Cahen, D., and Kahn, A. (2019). Halide perovskites: is it all about the interfaces? Chem. Rev. 119, 3349–3417.

Shin, S.S., Yeom, E.J., Yang, W.S., Hur, S., Kim, M.G., Im, J., Seo, J., Noh, J.H., and Seok, S.I. (2017). Colloidally prepared La-doped BaSnO$_3$ electrodes for efficient, photostable perovskite solar cells. Science 356, 167–171.

Stranks, S.D., Eperon, G.E., Grancini, G., Menelaou, C., Alcocer, M.J.P., Leijtens, T., Herz, L.M., Petrozza, A., and Snaith, H.J. (2013). Electron-hole diffusion lengths exceeding 1 micrometer in an organometal trihalide perovskite absorber. Science 342, 341–344.

Tan, H., Jain, A., Voznyy, O., Lan, X., García de Arquer, F.P., Fan, J.Z., Quintero-Bermudez, R., Yuan, M., Zhang, B., Zhao, Y., et al. (2017). Efficient and stable solution-processed planar

perovskite solar cells via contact passivation. Science 355, 722–726.

Tang, P., Liu, C., Zhang, J., Wu, L., Wei, L., Feng, L., Zeng, G., and Wang, W. (2018). Surface modification effects of fluorine-doped tin dioxide by oxygen plasma ion implantation. Appl. Surf. Sci. 436, 134–140.

Tress, W., Correa Baena, J.P., Saliba, M., Abate, A., and Graetzel, M. (2016). Inverted current-voltage hysteresis in mixed perovskite solar cells: polarization, energy barriers, and defect recombination. Adv. Energy Mater. 6, 1600396.

Wang, C., Zhao, D., Grice, C.R., Liao, W., Yu, Y., Cimaroli, A., Shrestha, N., Roland, P.J., Chen, J., Yu, Z., et al. (2016). Low-temperature plasma-enhanced atomic layer deposition of tin oxide electron selective layers for highly efficient planar perovskite solar cells. J. Mater. Chem. A 4, 12080–12087.

Wang, Z., Lin, Q., Chmiel, F.P., Sakai, N., Herz, L.M., and Henry, J.S. (2017a). Efficient ambient-air-stable solar cells with 2D-3D heterostructured butylammonium-caesium- formamidinium lead halide perovskites. Nat. Energy 2, 17135.

Wang, X., Wang, X., Di, Q., Zhao, H., Liang, B., and Yang, J. (2017b). Mutual effects of fluorine dopant and oxygen vacancies on structural and luminescence characteristics of F doped SnO$_2$ nanoparticles. Materials (Basel) 10, 1398.

Wang, Y., Duan, C., Li, J., Han, W., Zhao, M., Yao, L., Wang, Y., Yan, C., and Jiu, T. (2018a). Performance enhancement of inverted perovskite solar cells based on smooth and compact PC$_{61}$BM: SnO$_2$ electron transport layers. ACS Appl. Mater. Interfaces 10, 20128–20135.

Wang, C., Zhang, C., Wang, S., Liu, G., Xia, H., Tong, S., He, J., Niu, D., Zhou, C., Ding, K., et al. (2018b). Low-temperature processed, efficient, and highly reproducible cesium-doped triple cation perovskite planar heterojunction solar cells. Sol. RRL 2, 1700209.

Wei, J., Guo, F., Wang, X., Xu, K., Lei, M., Liang, Y., Zhao, Y., and Xu, D. (2018). SnO$_2$-in-polymer matrix for high-efficiency perovskite solar cells with improved reproducibility and stability. Adv. Mater. 30, 1805153.

Xie, J., Huang, K., Yu, X., Yang, Z., Xiao, K., Qiang, Y., Zhu, X., Xu, L., Wang, P., Cui, C., et al. (2017). Enhanced electronic properties of SnO$_2$ via electron transfer from graphene quantum dots for efficient perovskite solar cells. ACS Nano 11, 9176–9182.

Xiong, L., Guo, Y., Wen, J., Liu, H., Yang, G., Qin, P., and Fang, G. (2018). Review on the application of SnO$_2$ in perovskite solar cells. Adv. Funct. Mater. 28, 1802757.

Yang, D., Yang, R., Zhang, J., Yang, Z., Liu, S., and Li, C. (2015). High efficiency flexible perovskite solar cells using superior low temperature TiO$_2$. Energy Environ. Sci. 8, 3208–3214.

Yang, D., Zhou, X., Yang, R., Yang, Z., Yu, W., Wang, X., Li, C., Liu, S., and Chang, R.P.H. (2016). Surface optimization to eliminate hysteresis for record efficiency planar perovskite solar cells. Energy Environ. Sci. 9, 3071–3078.

Yang, G., Wang, C., Lei, H., Zheng, X., Qin, P., Xiong, L., Zhao, X., Yan, Y., and Fang, G. (2017). Interface engineering in planar perovskite solar cells: energy level alignment, perovskite morphology control and high performance achievement. J. Mater. Chem. A 5, 1658–1666.

Yang, Z., Dou, J., and Wang, M. (2018a). Interface engineering in n-i-p metal halide perovskite solar cells. Sol. RRL 2, 1800177.

Yang, D., Yang, R., Wang, K., Wu, C., Zhu, X., Feng, J., Ren, X., Fang, G., Priya, S., and Liu, S. (2018b). High efficiency planar-type perovskite solar cells with negligible hysteresis using EDTA-complexed SnO_2. Nat. Commun. 9, 3239.

Yu, H., Yeom, H.-I., Lee, J.W., Lee, K., Hwang, D., Yun, J., Ryu, J., Lee, J., Bae, S., Kim, S.K., et al. (2018). Superfast room-temperature activation of SnO_2 thin films via atmospheric plasma oxidation and their application in planar perovskite photovoltaics. Adv. Mater. 30, 1704825.

Zhou, H., Chen, Q., Li, G., Luo, S., Song, T.-b., Duan, H.-S., Hong, Z., You, J., Liu, Y., and Yang, Y. (2014). Interface engineering of highly efficient perovskite solar cells. Science 345, 542–546.

Zhu, Z., Ma, J., Wang, Z., Mu, C., Fan, Z., Du, L., Bai, Y., Fan, L., Yan, H., Phillips, D.L., et al. (2014). Efficiency enhancement of perovskite solar cells through fast electron extraction: the role of graphene quantum dots. J. Am. Chem. Soc. 136, 3760–3763.

Zhu, Z., Bai, Y., Liu, X., Chueh, C.-C., Yang, S., and Jen, A.K.-Y. (2016). Enhanced efficiency and stability of inverted perovskite solar cells using highly crystalline SnO_2 nanocrystals as the robust electron-transporting layer. Adv. Mater. 28, 6478–6484.

Zuo, L., Chen, Q., De Marco, N., Hsieh, Y.-T., Chen, H., Sun, P., Chang, S.-Y., Zhao, H., Dong, S., and Yang, Y. (2017). Tailoring the interfacial chemical interaction for high-efficiency perovskite solar cells. Nano Lett. 17, 269–275.
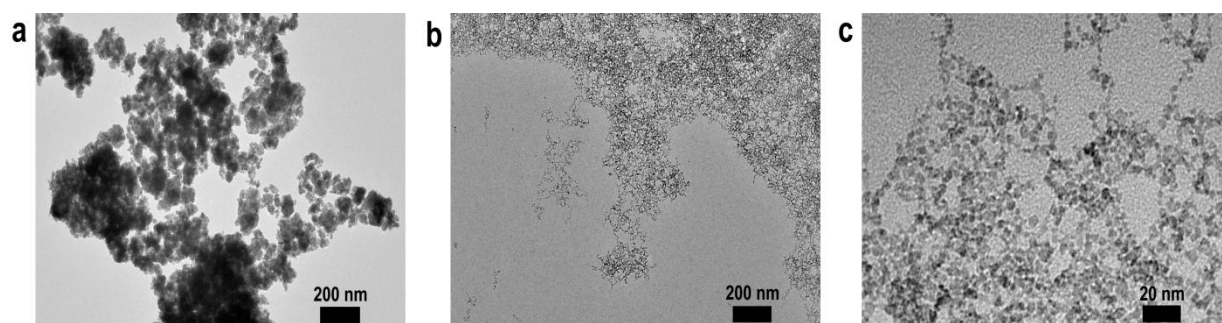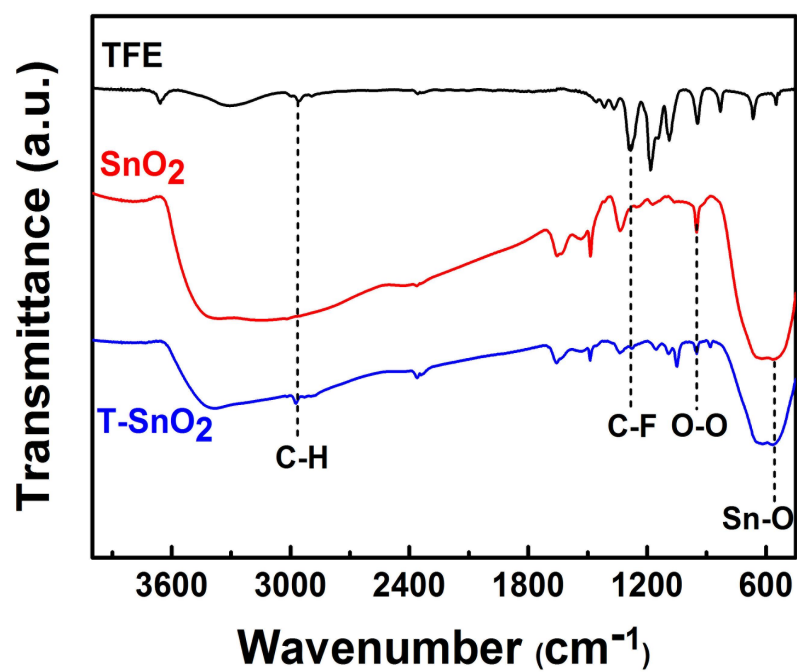
Supplemental Information

High-Performance Planar Perovskite Solar

Cells with Negligible Hysteresis Using

2,2,2-Trifluoroethanol-Incorporated SnO$_2$

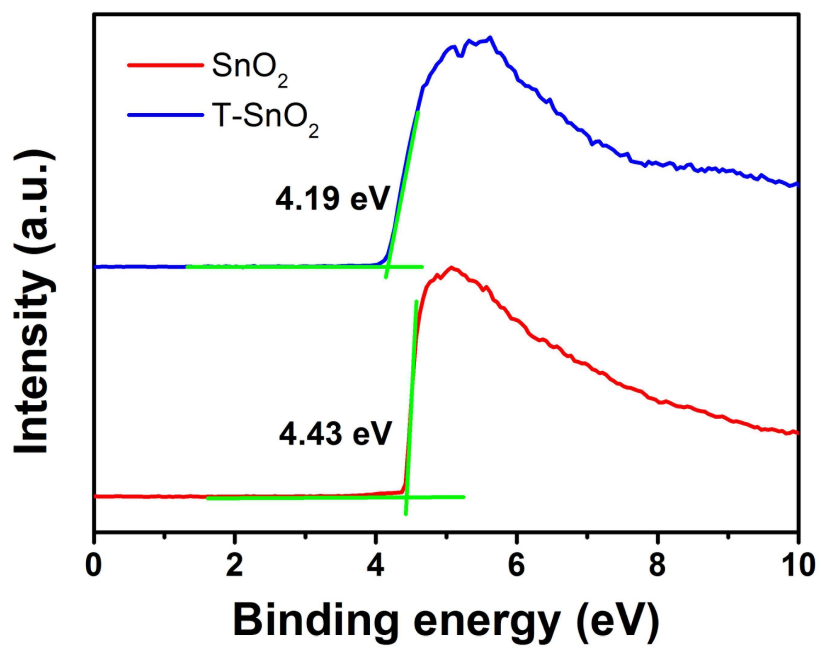Yigang Luan, Xiaohui Yi, Peng Mao, Yuanzhi Wei, Jing Zhuang, Ningli Chen, Tao Lin, Cheng Li, and Jizheng Wang

Supplemental Information

Figure S1 TEM images of the a) SnO_2 and b,c) T-SnO_2 nanoparticles. Related to figure 1.
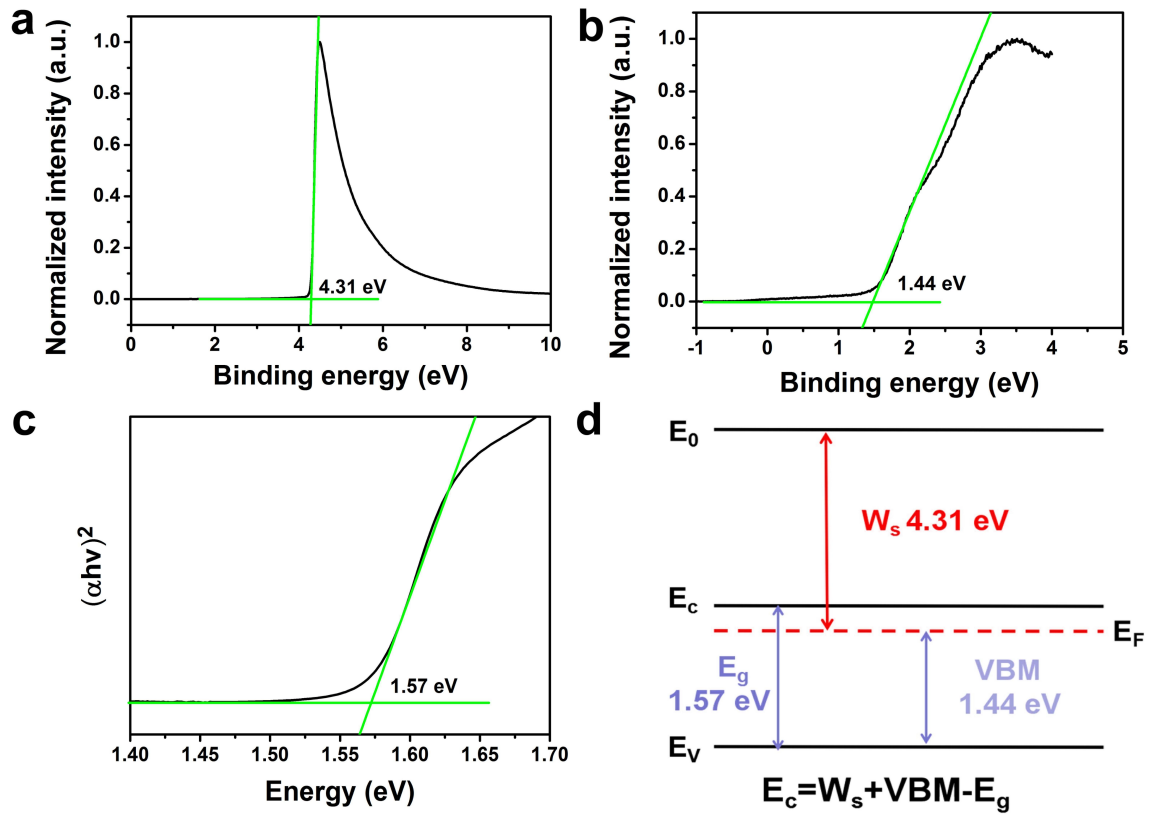
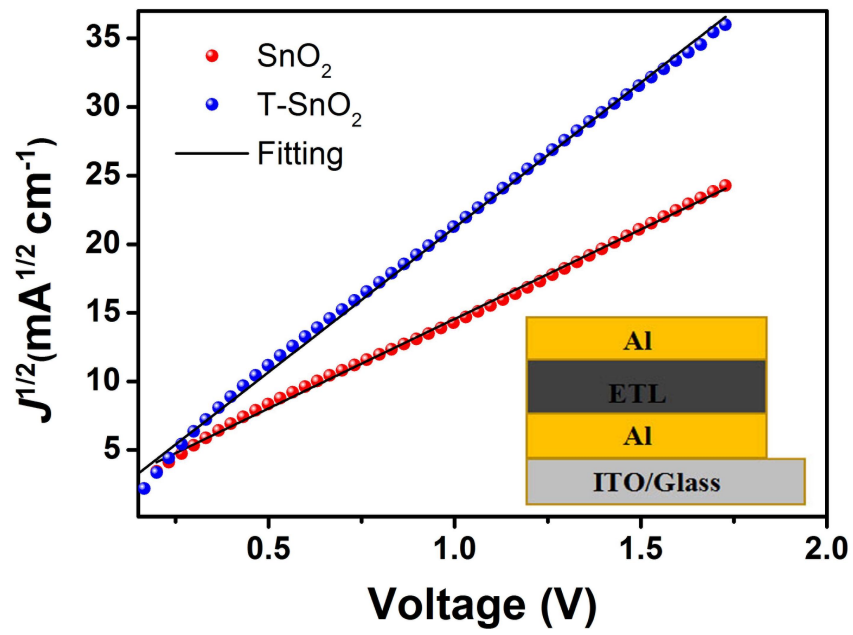**Figure S2** FTIR spectra of the TFE, SnO_2 and T-SnO_2 films. Related to figure 1A and 1B.

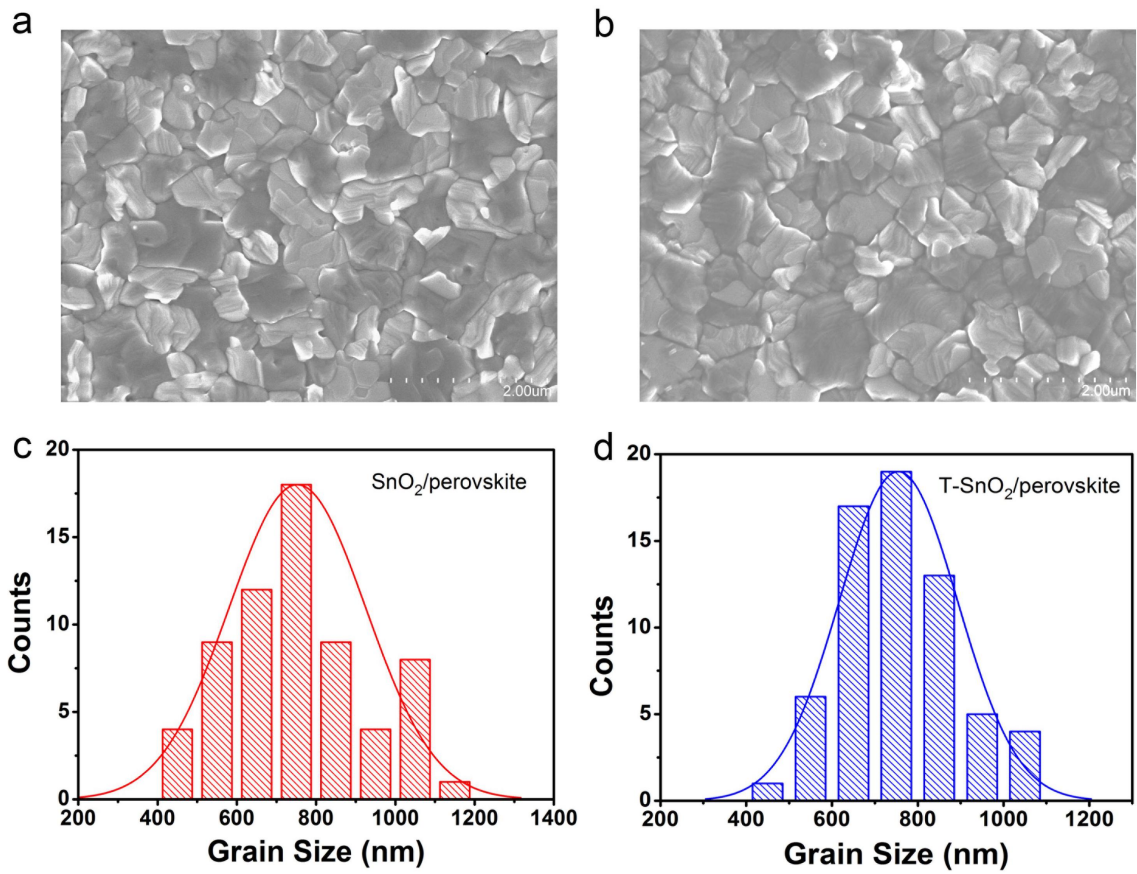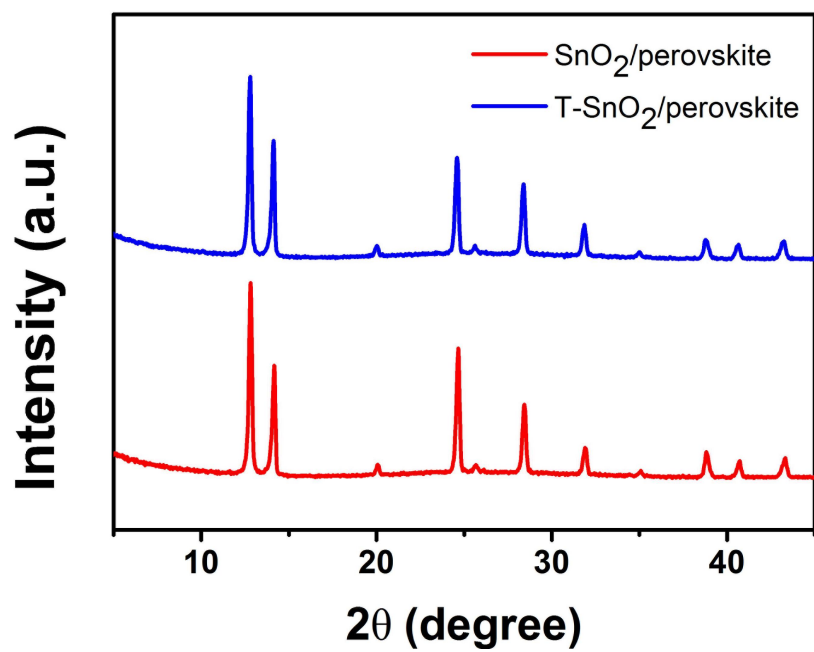**Figure S3** The UPS cut-off edge of the SnO_2 and $T-SnO_2$ films. Relate to figure 1D.

Figure S4 The UPS data of the perovskite film. a) the cut-off edge. b) Valence band. c) Bandgap. d) band structure. It can be calculated that the conduction band (E_c) of the perovskite is 4.18 eV. Relate to figure 1D.

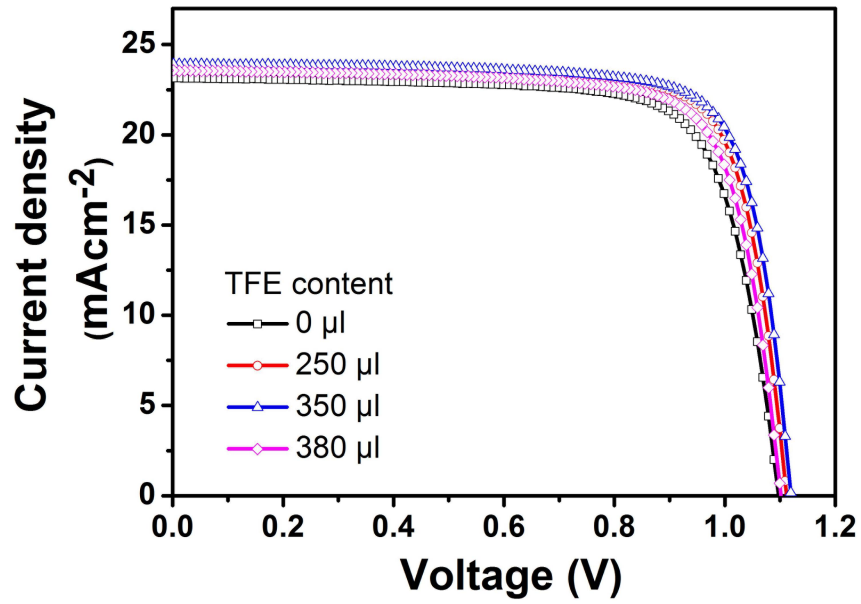**Figure S5** The electron mobility for the SnO₂ and T-SnO₂ films calculated by the SCLC model with the device structure of Glass/ITO/Al/ETL/Al. Related to figure 1.

Figure S6 The morphology of perovskite deposited on the SnO_2 and $T-SnO_2$ substrates. Top-view SEM images and the grain size distribution of perovskite coated on a,c) SnO_2 and b,d) $T-SnO_2$. Related to figure 2.
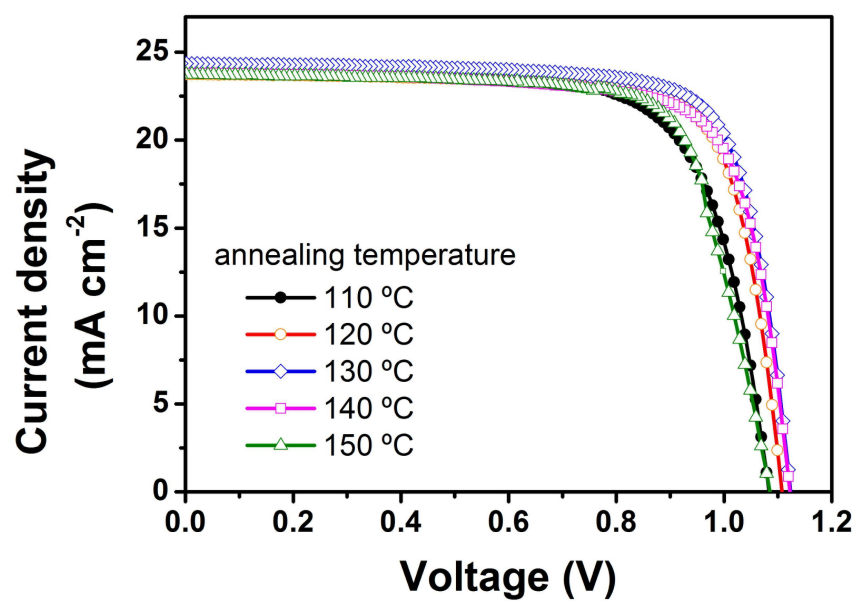
Figure S7 XRD spectra of the perovskite film grown on the SnO_2 and T-SnO_2 ETLs. Related to figure 2.
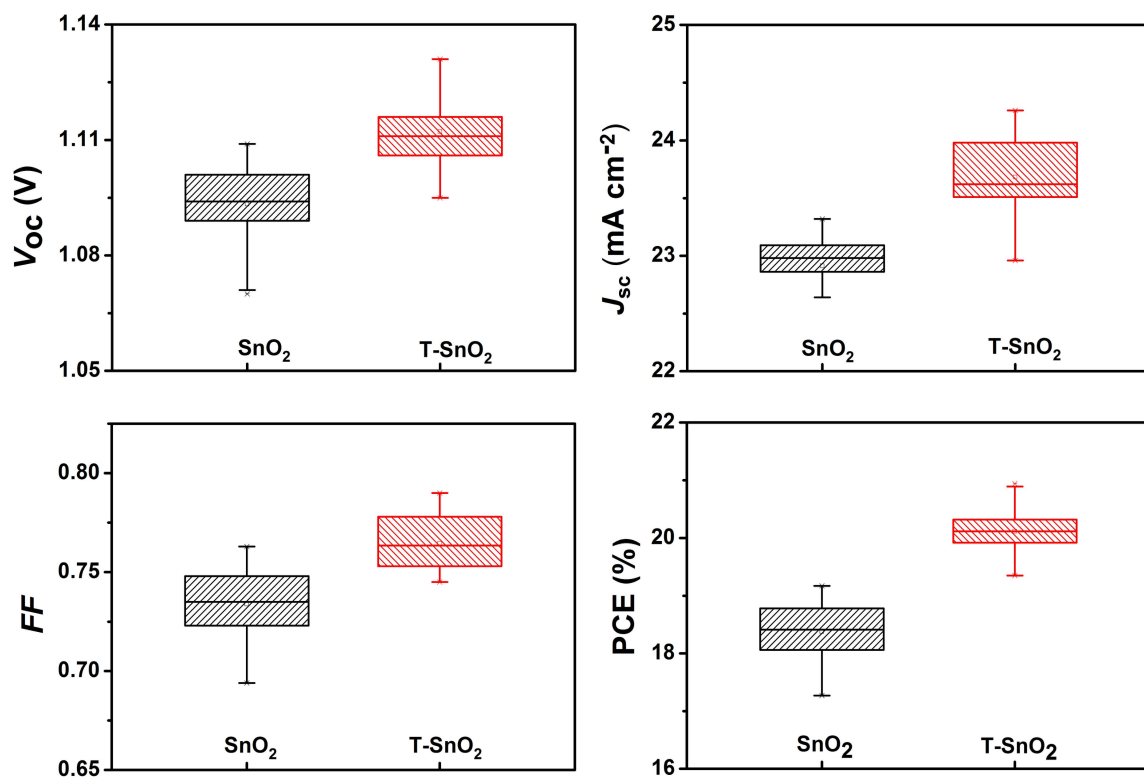
Figure S8 *J-V* curves of the PSCs based on the T-SnO$_2$ ETLs. T-SnO$_2$ ETLs with various TFE contents in the SnO$_2$ solution. The solar cells show the optimum performance at the TFE volume of 350 μl. Related to figure 2B.
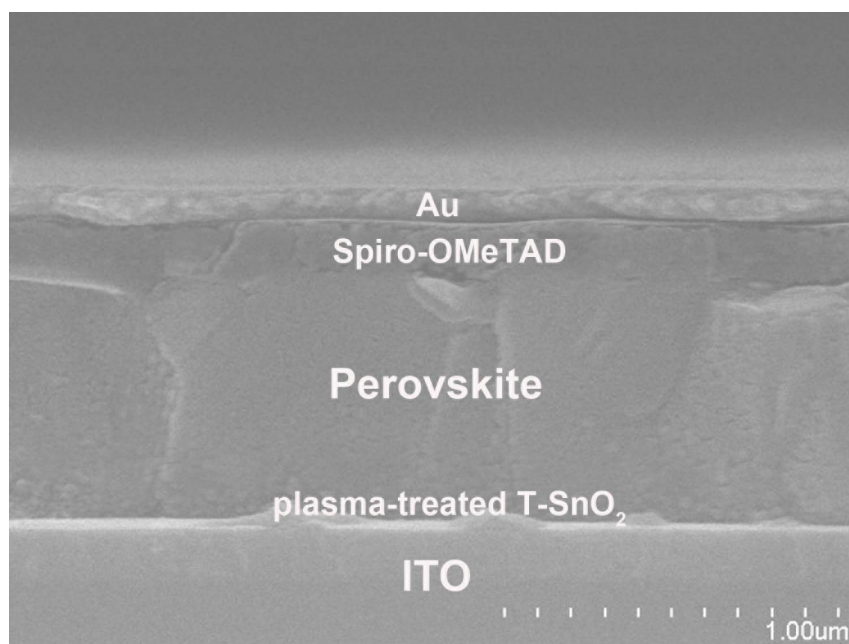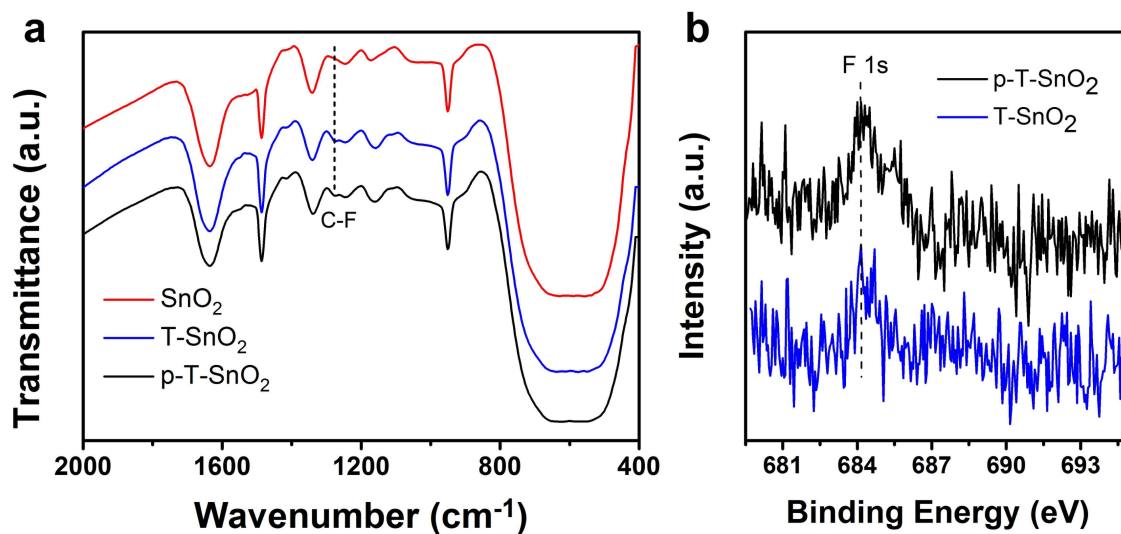
Figure S9 *J-V* curves of the PSCs based on the T-SnO$_2$ ETLs. T-SnO$_2$ ETLs with various annealing temperatures. The solar cells show the best performance at the annealing temperature of 130°C. Related to figure 2B.
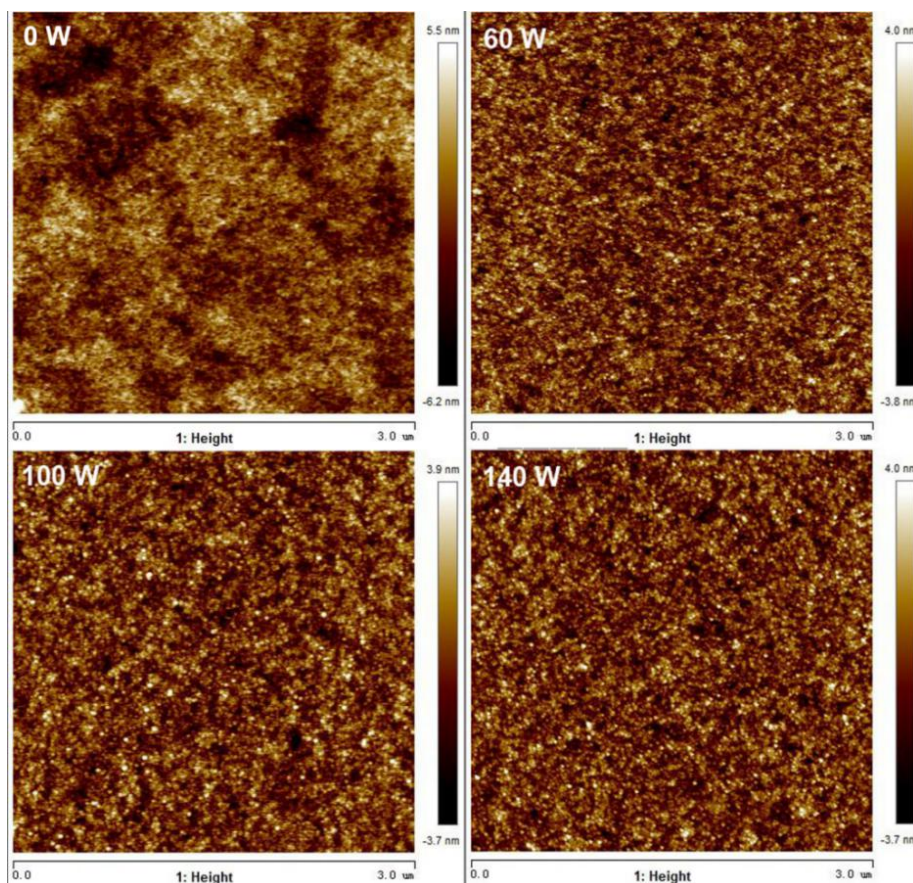
Figure S10 Comparison of photovoltaic parameters for the SnO₂ and T-SnO₂ devices. There were 50 cells for each counted from 10 different batches. All the data are from reverse scan. Related to figure 2C.

Figure S11 SEM cross-sectional image of the p-T-SnO$_2$ device. Related to figure 4A.

Figure S12 a) FTIR spectra of the SnO_2, $T\text{-}SnO_2$ and $p\text{-}T\text{-}SnO_2$ films. b) XPS spectra of the F 1s peaks for the $T\text{-}SnO_2$ and $p\text{-}T\text{-}SnO_2$ films. Related to figure 4.

Figure S13 The AFM images of the T-SnO$_2$ films (with different plasma powers). Note that the 0 W condition is T-SnO$_2$ without any plasma treated. Related to figure 4B.

Figure S14 The UPS cut-off edge of the T-SnO$_2$ films (with different plasma powers). Related to figure 4B.

Figure S15 The XPS spectra of F 1s peaks of T-SnO$_2$ films without any treatment, with DMSO washed and washed with DMSO after depositing perovskite on the T-SnO$_2$ films. and once fluorine entered into the perovskite lattice from the T-SnO$_2$/perovskite interface, it could be dissolved in DMSO. Related to figure 1A.

Table S1 Photovoltaic parameters of the PSCs with different ETLs. Related to figure 2B.

ETL	Scan direction	V_{oc} (V)	J_{sc} (mA cm^{-2})	*FF* (-)	PCE (%)
SnO$_2$	Reverse	1.10	23.12	0.755	19.17
	Forward	1.06	23.03	0.674	16.47
100-T-SnO$_2$	Reverse	1.10	23.51	0.756	19.55
	Forward	1.06	23.43	0.703	17.49
250-T-SnO$_2$	Reverse	1.11	23.74	0.779	20.57
	Forward	1.08	23.69	0.757	19.33
350-T-SnO$_2$	Reverse	1.12	23.91	0.780	20.92
	Forward	1.11	23.87	0.777	20.62
380-T-SnO$_2$	Reverse	1.10	23.55	0.767	19.88
	Forward	1.09	23.54	0.766	19.71

Table S2 Parameters of the TRPL spectra of perovskite deposited on different substrates. Related to figure 3C.

Sample	τ_{ave}/ns	τ_1/ns	*A$_1$*	τ_2/ns	*A$_2$*
Glass/perovskite	763.36	303.56	41.68	890.16	51.54
SnO$_2$/perovskite	146.89	61.73	34.74	164.11	64.60
T-SnO$_2$/perovskite	52.39	10.65	35.60	56.64	65.74

Table S3 EIS parameters of the SnO$_2$ and T-SnO$_2$ devices. Related to figure 3D.

Substrates	R_s (Ω)	R_{tr} (Ω)	C_{tr} (Ω)	R_{rec} (Ω)	C_{rec} (Ω)
SnO$_2$	29.9	56.4	5.781E-8	294.2	1.056E-8
T-SnO$_2$	27.6	36.8	8.419E-8	650.5	4.480E-8

Table S4 Photovoltaic parameters of the p-T-SnO$_2$ devices with different plasma powers at fixed O$_2$ gas flow rate of 0.05 L h^{-1}. Related to figure 4B.

Style	Power (W)	V_{oc} (V)	J_{sc} (mA cm^{-2})	*FF* (-)	PCE (%)
	0	1.12	23.91	0.780	20.92
	60	1.12	24.06	0.802	21.68
Oxygen plasma	100	1.10	24.00	0.795	21.07
	140	1.07	23.92	0.796	20.35

Table S5 Roughnesses of the p-T-SnO$_2$ films with different plasma powers at fixed O$_2$ gas flow rate of 0.05 L h^{-1}. The scan size of all the films is 3 um. The roughness is almost 32% lower than original one (pure T-SnO2), and when the power increased from 60 W to 140 W, the variation in roughness is negligible. Related to figure 4.

Plasma power (W)	R_q (nm)	R_a (nm)	R_{max} (nm)
0 W	1.67	1.27	14.2
60w	1.13	0.89	12.1
100W	1.09	0.86	12.6
160W	1.08	0.86	11.2

Table S6 Work functions of the p-T-SnO$_2$ films with different plasma powers at fixed O$_2$ gas flow rate of 0.05 L h^{-1}. Related to figure 4.

Plasma power (W)	0	60	100	140
Work function (eV)	4.19	4.21	4.34	4.40

Transparent Methods

Precursor SnO₂ and T-SnO₂ Solution

The SnO₂ precursor solution was obtained by diluting the SnO₂ colloidal solution (the concentration is 2.67%). For T-SnO₂ solution, the 2,2,2-Trifluoroethanol (aladdin) was added into the distilled water and fully stirred (the total volume is 650 μl). After that, the SnO₂ colloidal solution (100 μl) was added into the mixed solution. The solution was then heated to 32°C and stirred about 30 min to form T-SnO₂ solution.

Fabrication of Solar Cells

The glass/ITO was washed in the order of cleanser essence, distilled water, acetone and isopropyl alcohol for 30 min. For the SnO₂ ETL, the precursor solution was spin-coated onto the ITO at 3500 rpm for 35 s, and then annealed at 150 °C for 30 min. For the T-SnO₂ ETL, the precursor solution was spin-coated onto the ITO at 3500 rpm for 35 s, and then annealed at 130 °C for 30 min. For the p-T-SnO₂ ETL, the T-SnO₂ ETL surface was treated by O₂ plasma for 5 min with various powers at a fixed O₂ flow rate of 0.05 L h⁻¹. The perovskite film was made by two-step method. For the first step, 760 mg PbI₂ was added into 1 ml DMF and 160 μl DMSO mixed solution, then was stirred over night at 25°C. The as-prepared solution was used as PbI₂ layer by spin-coating at 1600 rpm for 23 s and then 4000 rpm for 27 s, Then annealed at 70°C for 2 min. For the second step, the FAI: MACl: MABr mixed solution (110: 11: 11.5 mg in 1.5 ml isopropyl alcohol) was spin-coated onto the PbI₂ layer at 2000 rpm for 23 s, then the sample was taken out of the glove box and annealed at 140 °C for 20 min (ambient air,~ 40% humidity). After annealing, the sample was rapidly transferred to the glove box for HTL coating. The Spiro-OMeTAD (72.3 mg) in chlorobenzene (CB) solution (1 ml), adding 17.5 μl Li-TFSI/acetonitrile mixed solution (170 mg ml⁻¹) and 28.8 μl 4-tBP, which was coated at 4000 rpm for 27 s. After that, the sample was stored in the drying cabinet (ambient air, ~1% humidity) for 20 h. Finally, 90 nm Au electrode was deposited by vacuum evaporation at the pressure of 3×10⁻⁶ Torr.

Thin Film Characterization

UPS and XPS tests were performed on XPS machine (ESCALAB250XI, Thermo Fisher Scientific). The XRD patterns were obtained to research the crystallographic characteristics of perovskite, which was measured by using Rigaku-2500 X-ray diffractometer with CuKα radiation, λ =1.5406 Å. The surface morphology and cross section of the devices are investigated by SEM (S-4800, Japan). The surface roughness of the electron transfer layers were obtained by using atomic force microscope (AFM, Bruker MultiMode 8 SPM system).

Electron Mobility Calculation

The electron mobilities of SnO₂ and T-SnO₂ films were calculated by the SCLC method. The Equation is below:

$$J = \frac{9}{8}\mu_e \varepsilon_0 \varepsilon_r \frac{V^2}{L^3}$$

Where μ_e, ε_0, ε_r and L are electron mobility, free space permittivity, dielectric constant and the thickness of electron transport layer.

Average Carrier Lifetime Calculation

The carrier lifetime (τ_{ave}) can be calculated using the Equation:

$$\tau_{ave} = \frac{\sum A_i \tau_i^2}{\sum A_i \tau_i}$$

where A_i and τ_i are the decay amplitude and decay time.

Device Characterization

All *J-V* curves were measured using the Keithley 2420, and the solar cell was illuminated by a solar simulator (Newport 94043A, AM 1.5G, USA). The light intensity was calibrated by the monocrystalline silicon reference cell with a standard value 100 mW cm^{-2}. The device area was 0.044 cm^2. The external quantum efficiency (EQE) spectra was obtained with Newport 300 W Xenon Light Source (Newport IQE 200, USA). The electrical impedance spectroscopy (EIS) was measured by Zennium (Zahner).